RSC Advances

PAPER



Cite this: *RSC Adv.*, 2022, **12**, 9112

# Novel Au nanorod/$Cu_2O$ composite nanoparticles for a high-performance supercapacitor†

Hansa Mahajan and Seongjae Cho *

Metal–oxide nanomaterials have attracted great interest in recent years due to their novel characteristics such as surface effect and quantum confinement. A fascinating Au nanorod (NR)/cuprous oxide core–shell composite (AuNR/$Cu_2O$) was directly synthesized using a moderate one-pot facile green redox method and further utilized for energy storage applications in a supercapacitor. The synthesis mechanism is based on the use of reducing agents to form the core shell. The resultant composite was deposited on the surface of nickel foam as a result of redox reactions between Au and Cu *via* a hydrothermal method. AuNR/$Cu_2O$ composite nanoparticles (NPs) were characterized using various spectroscopic and microscopic techniques, including UV-vis and X-ray photoelectron spectroscopies, Brunauer–Emmett–Teller surface area analysis, X-ray diffractometry, and transmission electron microscopy. The AuNR/$Cu_2O$ composite NPs grow *via* the depositing of a 20–50 nm $Cu_2O$ shell on an AuNR core with dimensions of 5–20 nm in width and 40–70 nm in length. The as-synthesized AuNR/$Cu_2O$ composite NPs were effectively used as electrode materials in a supercapacitor, and their electrochemical performance was determined by cyclic voltammetry, galvanostatic charge–discharge measurements, and electrochemical impedance spectroscopy in 2 M KOH aqueous solution as an electrolyte. The composite NPs showed excellent average specific capacitance of 235 F $g^{-1}$ at a current density of 2 A $g^{-1}$ and durable cycling stability (96% even after 10 000 cycles). The higher efficiency of the AuNR/$Cu_2O$ composite NPs can be attributed to the presence of AuNR in the core. The AuNR/$Cu_2O$ composite NPs exhibit a high surface area and high electrical conductivity, which consequently result in their excellent specific capacitance and outstanding rate as an all-solid-state supercapacitor electrode.

Received 7th February 2022
Accepted 8th March 2022

DOI: 10.1039/d2ra00812b

rsc.li/rsc-advances

## 1. Introduction

The current energy crisis and environmental pollution are serious global concerns that have led to the growing demand for new storage technologies and sustainable energy materials. From this perspective, supercapacitors hold potential to be high-tech storage devices and promise to be a sustainable approach owing to their great energy and power density, fast charging–discharging ability, and long life cycle.[1–4] Based on charge storage mechanisms, supercapacitors can be categorized into two types: pseudocapacitors and electrical double-layer capacitors (EDLCs).[5] Pseudocapacitors show superior specific capacity and excellent power density compared with EDLCs due to the quick reversible faradaic responses of their conductor materials, principally together with oxides,[6] metal–oxides,[7] carbon-based materials, and polymers.[8] Amongst the diverse anode and cathode materials used as pseudocapacitors, metal or metal–oxide-based composites remain the best electrodes in terms of high energy efficiency due to their distinct electrochemical redox performances, high specific capacitance, and cost-effectiveness.[9–11] Over the past few years, a range of extremely conductive nano-materials, such as graphene, carbon nanotubes, carbon nano-onions, and other metallic nano-composites, have been synthesized through metal oxidization to enhance their conductivity.[12,13] Metal nanoparticles (NPs) exhibit excellent electrochemical performance and a high effective surface area. Several metal oxide composites, including flower-like materials,[14] nanorods (NRs),[15–17,] and nanowires,[18] have been reported. Furthermore, the morphological structure and configuration of metal oxides play a major role in the electrochemical properties of the acquired material. The element position, particle size, and volume of the external oxygen species have a direct impact on the morphology and structure of the composite material, which in turn affect the efficiency of a material.[19] Therefore, a large number of studies have detailed the synthesis of gold NRs *via* a seed-growth method using cuprous oxide with a tunable morphology and pore size.

In this work, Au/$Cu_2O$ composite NPs were successfully synthesized *via* a one-pot redox process. This research then describes the synthesis, characterization, and energy storage

*Department of Electronics Engineering, Gachon University, Republic of Korea. E-mail: felixcho@gachon.ac.kr*

† Electronic supplementary information (ESI) available. See DOI: 10.1039/d2ra00812b

applicability of the synthesized AuNR/$Cu_2O$ composite NPs. Excellent electrochemical performance was achieved *via* the combination of $Cu_2O$ and Au in the supercapacitor. The Au/$Cu_2O$ composite NPs exhibited superb performances towards supercapacitor applications owing to the synergistic effect between the Au NPs and $Cu_2O$. Moreover, the Au/$Cu_2O$ composite NPs demonstrated high surface area and porosity. A high surface area and pores provide a great route for electrolyte in energy storage electrodes towards supercapacitor applications. With electrochemical characteristics including enhanced electrical properties and surface area, the Au/$Cu_2O$ is considered to be a promising electrode material for use in high-performance energy devices.

## 2. Results and discussion

### 2.1 Structure and morphological analysis

Transmission electron microscopy (TEM) and high-resolution (HRTEM), selected area electron diffraction (SAED), scanning TEM (STEM) and elemental mapping analysis were carried out, with the results presented in Fig. 1. The AuNR size is in the range of 5–50 nm, whereas the thickness of the $Cu_2O$ nanocubes (NCs) is in the range of 50–100 nm, and the size of the Au/$Cu_2O$ composite is in the range of 50–100 nm. From Fig. 1(a) and (b), the size of the AuNRs ranges between 5 and 50 nm depending on the direction. Fig. 1(c) shows the STEM elemental mapping of Au in the NR structure, which confirms that Au is present in the nanoparticles. The SAED pattern in Fig. 1(d) reveals the crystallinity of the atomic arrangements in the AuNRs. Fig. 1(e)–(h) show the TEM, HRTEM, STEM elemental mapping, and SAED pattern analysis results of the $Cu_2O$ NCs. Fig. 1(e) shows that the $Cu_2O$ NCs have a uniform shape with an edge length of approximately 80 nm. Fig. 1(f) shows a single $Cu_2O$ NC that is lying on its (100) face. Fig. 1(g) shows the STEM elemental mapping which confirms the presence of Cu in the $Cu_2O$ NCs. Fig. 1(h) shows the SAED pattern, in which the pattern reveals that the crystallographic zone axis is [001] and confirmation of a nanocube structure. In the same order, Fig. 1(i)–(l) demonstrates the microscopic examination, elemental analysis, and crystallinity analysis results of the Au/$Cu_2O$ composite. Fig. 1(i) confirms the formation of a homogeneous NR core–shell structure. The sizes of the Au core and $Cu_2O$ shell are approximately 100 nm, respectively. The average size of the pure AuNR is smaller than the $Cu_2O$ shell in the composite of Au/$Cu_2O$. It can be observed that there is contrast between dark (Au) and lighter ($Cu_2O$) regions, identifying the formation of the Au/$Cu_2O$

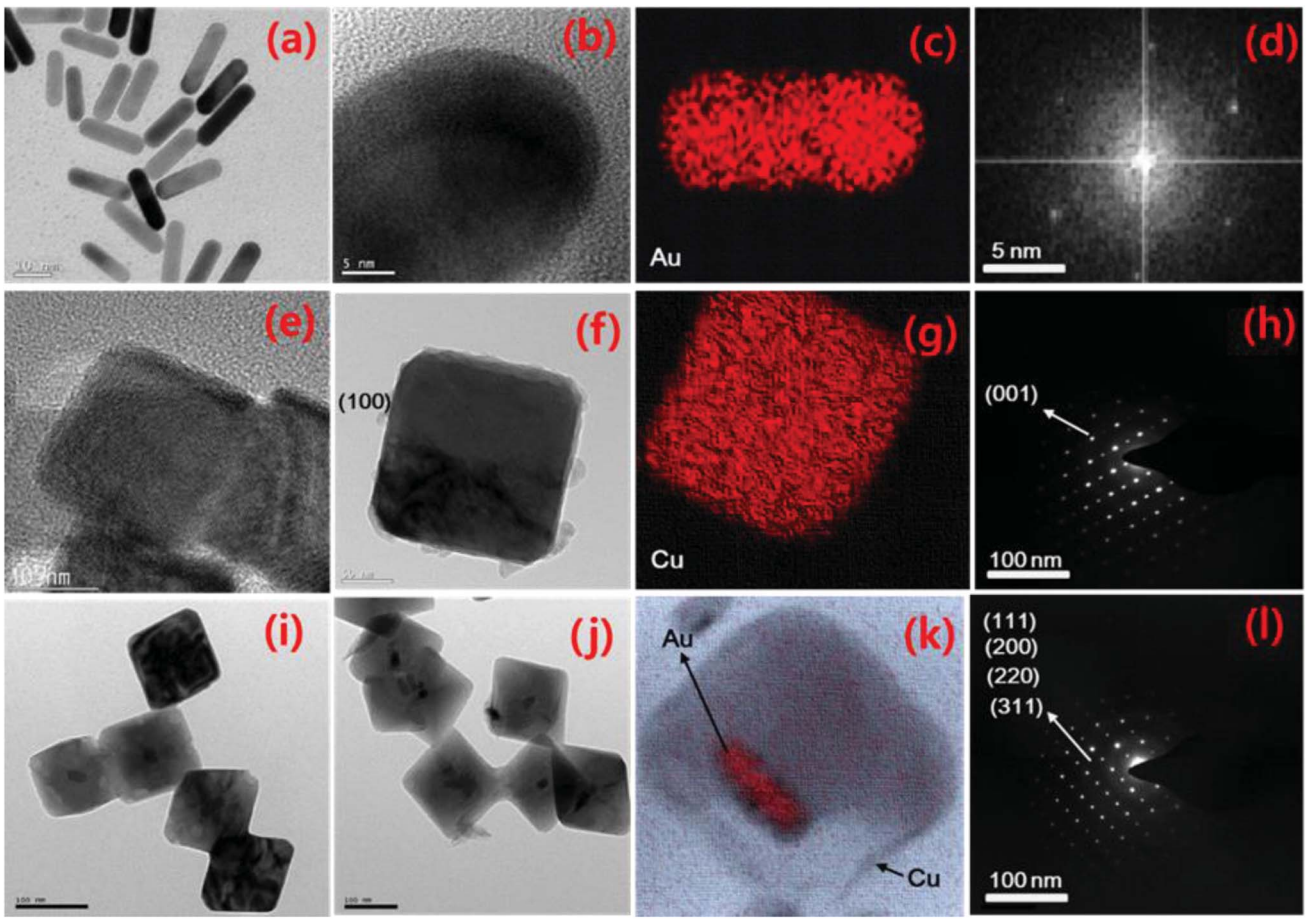


Fig. 1 Nanostructure analysis results. TEM, HRTEM, STEM elemental mapping, and SAED pattern analyses of the (a–d) AuNR structure, (e–h) $Cu_2O$ NC structure, and (i–l) Au/$Cu_2O$ core–shell heterostructure.

composite and further corroborating the elemental mapping in Fig. 1(k). The SAED pattern of the Au/$Cu_2O$ composite is shown in Fig. 1(l), which confirms that the $Cu_2O$ core–shell is polycrystalline in nature. The energy-dispersive X-ray spectroscopy (EDX) analysis results for Cu, Au, and O are additionally provided in Fig. S1.† The bright-field image of the composite confirms that the $Cu_2O$ NCs are covered with Au NPs, making up the core–shell structure. The as-prepared nanocomposite is interconnected in a homogeneous way so that low resistance during electrolyte diffusion is expected but fast ion and electron transport for faradaic reaction also occur.[20]

### 2.2 Optical and BET analysis

The UV-vis spectrum of the resultant NPs is shown in Fig. 2(a). The absorption peaks for the $Cu_2O$ NCs and Au/$Cu_2O$ composite NPs are present at 489 and 508 nm, respectively. The absorption band at 489 nm is recognized as the band-edge absorption of the $Cu_2O$ NCs. The absorption of the AuNRs embedded in $Cu_2O$ is observed at 508 nm, which is not very intense due to the band-edge absorption of $Cu_2O$. The surface plasmon resonance spectra of gold materials are significantly red-shifted when they are covered by $Cu_2O$.[21–23] The $Cu_2O$ absorption appearances are differentiated due to their large sizes that cause solid light dispersion. The absorption of the Au/$Cu_2O$ composite NPs is more intense than that of $Cu_2O$. The Fourier-transfer infrared spectra of the $Cu_2O$ NCs and Au/$Cu_2O$ composite NPs are displayed in Fig. 2(b). The distinctive peak of Cu(I)–O observed at 631 $cm^{-1}$ reveals the structure of the $Cu_2O$ NCs. However, after the formation of the Au/$Cu_2O$ composite NPs, the intensity of the Au peak reduced and marginally red-shifted the vibrations of Au–O at 583 and 515 $cm^{-1}$, and these peaks can be attributed to the functional groups of the Au/$Cu_2O$ composite NPs. The minor blue-shift in the Cu–O vibration is feasibly a result of a small particle size.[24–26] The wide absorption around the peak at 3498 $cm^{-1}$ is attributed by O–H stretching with its peak at 1621 $cm^{-1}$ that is usually observed with bending in water molecules. Thus, only peaks for the as-synthesized Au/$Cu_2O$ composite were observed.

The resultant $Cu_2O$ and Au/$Cu_2O$ composite NPs were examined by X-ray diffractometry (XRD). Fig. 2(c) shows the XRD peaks of $Cu_2O$ and the Au/$Cu_2O$ composite NPs. The diffraction peaks can be seamlessly indexed to crystalline cubic cuprous oxide (cuprite) in terms of both position and relative intensity. The peaks at $2\theta$ values of 32.380°, 36.240°, 43.140°, 52.450°, and 64.400° represent the {110}, {100}, {200}, {211}, {311}, and {222} plane directions of the crystalline $Cu_2O$, correspondingly. The XRD pattern of the Au/$Cu_2O$ composite NPs reveals diffraction peaks located at $2\theta = 33.0°$, 36.0°, 42.8°, and 61.1°, which correspond to the {100}, {111}, {200}, and {222} plane directions of the plain cubic-phase $Cu_2O$ NCs. The other diffraction peaks located at 36.7°, 42.8°, 64.4°, and 78.1° can be respectively indexed to the {111}, {200}, {220}, and {311} planes of the face-centered cubic structure of the AuNRs. These results indicate that an ultrathin $Cu_2O$ shell is formed on the surface of the metallic AuNRs with neither amorphous nor additional phases.[27] XPS was used to identify the surface components on

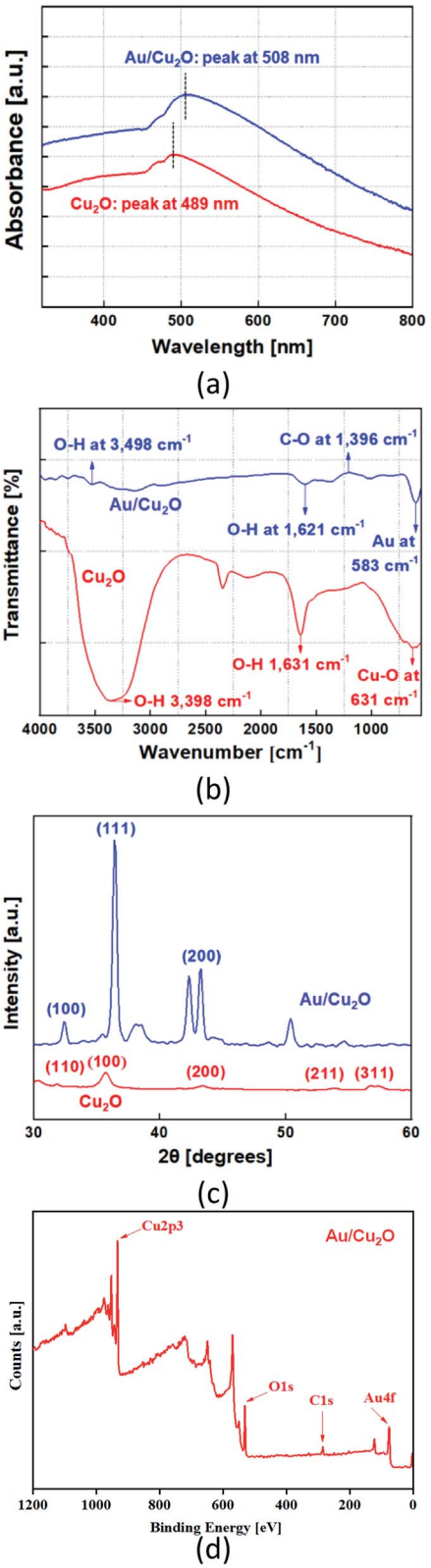


Fig. 2 Optical characterization of the nanostructures. (a) UV-vis absorption spectra, (b) FTIR spectra, and (c) powder XRD patterns of the $Cu_2O$ NC and Au/$Cu_2O$ composite NPs. (d) Survey XPS spectrum of the Cu2p, O1s, and Au4f of the core–shell Au/$Cu_2O$ NPs.

the shell. The survey XPS spectrum of the Au/$Cu_2O$ composite is presented in Fig. 2(d), which reveals peaks for the Cu2p, O1s, and Au as well as C1s of the Au/$Cu_2O$ composite. The presence of C1s and other peaks should be attributed to the residual capping agents on the particle surface. Generally, by using the peak of C1s at 284.8 eV, the binding energies were calibrated to reduce the charge effect of the samples. This suggests that the interfacial surface charge distribution of the Au/$Cu_2O$ composite changed and indicates the formation of a charge-transfer complex. This is explicit evidence of the strong interaction between Au and $Cu_2O$. The peak for $Cu2p_{3/2}$ in the XPS spectrum is at 932.6 eV as depicted in Fig. S2(i).† Cu is in the +1 oxidation state and is synchronized to the oxygen species, with a peak detected at 530.4 eV. The peak at 533.4 eV in the spectrum can be allocated to the oxygen species in the Cu–O bond, as supported by Fig. S2(ii).† The weak Au peaks from the AuNRs present in the ultrathin $Cu_2O$ shell are also detected, as can be confirmed from Fig. S2(iii).† The peaks are shifted towards a lower value compared to those of pure gold ($4f_{7/2}$ 84.2 eV and $4f_{5/2}$, 87.8 eV).[28] This shift appropriately corresponds to negatively charged AuNRs devoid of any chemical bonding with $Cu_2O$. The donor level of $Cu_2O$ is almost equal to the Fermi level of Au (5.4 eV). Thus, electron transfer from $Cu_2O$ to Au is possible, leading to an increase in the charge density on the surface of the AuNRs.

The $N_2$ adsorption isotherms of the $Cu_2O$ NCs and Au/$Cu_2O$ composite NPs exhibit an analogous type-II curve.[29] The Brunauer–Emmett–Teller (BET) effective areas of the $Cu_2O$ NC and Au/$Cu_2O$ composite NPs were found to be 14.870 $m^2\ g^{-1}$ and 1150.760 $m^2\ g^{-1}$, respectively, as shown in Fig. 3(a and b). The relative pressure ($P/P_0$) was in the range of 0.45–0.98 and the $N_2$ adsorption/desorption isotherms presented that the Au/$Cu_2O$ composite NPs showed the same type-IV curves, indicating a porous structure.[30,31] $Cu_2O$ has pores with a diameter of 156 nm (Fig. S3(a)†). However, the Au/$Cu_2O$ composite has pores with a diameter of 36 nm (Fig. S3(b)†) and a mesoporous network. The main reason for the high surface area is due to the presence of a structural internal surface of pores that are formed during the synthesis process shown in Schematic 1 in the ESI.† Ethanol probably serves as a pore-expanding agent in the synthesis.[32] Through combination with the hydrophilic group of the outer layer, ethanol occupies a certain space in the stacked structure. Under the action of combined surfactants, the AuNRs crystallize into smaller grains and aggregate into a highly porous structure, increasing their specific surface area. The results were verified by BET analysis, which indicated that the pore size decreased from 36 to 30 nm, as shown in Fig. S3(b).† The high specific surface area and pore size of the Au/$Cu_2O$ composite NPs results in them exhibiting a high specific capacitance. For a superior electrode in an energy device, a high effective surface area of a material usually presents extra active sites, which might eventually contribute towards an improvement in the performance of a supercapacitor. At the same time, the change in mass needs to be considered to contemplate the dramatic increase in the specific surface area, which has the unit of area per mass. Not only the increase in effective area but also the rapid decrease mass leads to a huge specific surface area.

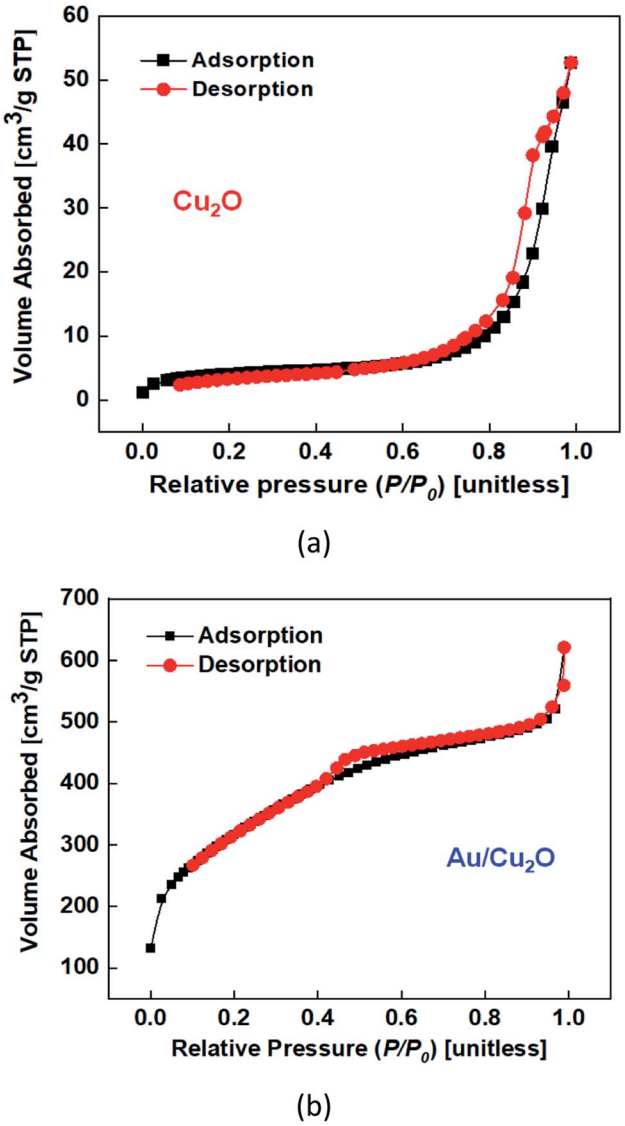


Fig. 3 Nitrogen adsorption and desorption isotherms of the (a) $Cu_2O$ NCs and (b) Au/$Cu_2O$ NPs.

### 2.3 Formation mechanism of the Au–$Cu_2O$ composite NPs

Firstly, pure $Cu_2O$ NCs were synthesized *via* the process detailed in the experimental Section 4.3. The entire synthesis is based on a redox reaction. Cu $(OH)_4^{2-}$ is initially shaped after adding NaOH to the $Cu_2O$ NCs. By altering the reductants and surfactants, diverse CuO nanoparticles of different types can be obtained. In addition to being a reducing agent, L-ascorbic acid also acts as a ligand, coordinating with $Cu^{2+}$ and forming the cube shell (Au/$Cu_2O$). The Au/$Cu_2O$ composite was produced using a combination of $CuCl_2$, sodium dodecyl sulfate (SDS), AuNRs, an aqueous solution of NaOH, and L-ascorbic acid. Identical shape and conformal growth of the $Cu_2O$ shells in the cubic structure were obtained. The function of SDS and

$Cu(OH)_4^{2-}$ species can also be understood. When the reducing agent is added to the solution, $Cu^{2+}$ is reduced to $Cu^{+}$. The role of ascorbic acid is to link the Cu $(OH)_4^{2-}$ species with the AuNRs, which promotes the hetero-evolution of $Cu_2O$. Additionally, increasing the volume of the Au nanocrystal solution added to the reaction mixture slowly decreases the size of the Au/$Cu_2O$ nanocrystals, and the resultant mixture determines the final nanoparticle size. Size controllability in comparable sizes of Au/$Cu_2O$ composites has been achieved using small AuNR cores, *via* a change in the amount of core Au. The essential redox process can be described using the following equations:

$$Cu^{2+} + 2OH^{-} \rightarrow Cu(OH)_2$$

$$2Cu(OH)_2 + C_6H_8O_6 \rightarrow Cu_2O + C_6H_6O_6 + 3H_2O$$

where $C_6H_6O_6$ is L-ascorbic acid, which is reduced in the chemical reaction. The success of the synthesis relies on the remaining amount of citrate ligands. Positively charged $Cu_2^{+}$ ions are attracted to the citrate ligands, which are negatively charged. Owing to $Cu^{2+}$–citrate binding, $Cu^{2+}$ is reduced at the surface of the AuNRs, forming an Au–$Cu_2O$ core–shell structure. The negatively charged citrate ligands keep the AuNRs separated and prevent their aggregation. The main reason for the $Cu_2O$ shell formation was $Cu^{2+}$ reduction by the reducing agent (ascorbic acid).

In the formation of the Au/$Cu_2O$ composite, a solution of AuNRs was used which contains $HAuCl_4$ used as the source material of the Au NRs. Electrostatic interactions may act as the driving force behind the absorption of the metal ions on the surface of $Cu_2O$. Finally, the adsorbed $AuCl_4$ ions were reduced and deposited randomly on the surface of $Cu_2O$ by ascorbic acid acting as a reducing agent. Although similar synthetic approaches have been used for Au deposition, the density of the deposited Au NPs was higher herein, presumably due to the higher affinity of $AuCl_4$ for the surface of $Cu_2O$. Hence, strong electrostatic interactions between the positively charged $Cu_2O$ and negatively charged $AuCl_4$ are expected, which results in a high density of Au NRs on the $Cu_2O$ NC surface. The driving force for Au deposition is very high. Therefore, it is understood well from our findings that ascorbic acid can be used as a reducing agent for the uniform deposition of Au NRs on the $Cu_2O$ surface.

## 3. Electrochemical measurements

A facile approach was proposed to grow $Cu_2O$ and Au/$Cu_2O$ composite NPs on the Ni foam substrate followed by an annealing treatment. The Au/$Cu_2O$ composite NPs were dropped onto the substrate and vacuum dried at 80 °C for 12 h. The mass of the material was calculated by increasing the areal mass density of the Ni foam after casting the electrode materials and was found to be in the range of 2–4 mg $cm^{-2}$. In this procedure, commercial Ni foam for the substrate was applied as a current collector. Cleaning was performed using acetone, hydrochloric acid, deionized water, and ethanol in sequence. The Cu wires were attached to the material surface using silver paste to make the electrodes at the same time. The supercapacitor was assembled with a structure of two electrodes separated, which was soaked in an aqueous electrolyte of 2 M KOH solution. Electrochemical measurements of the $Cu_2O$ NCs and Au/$Cu_2O$ composite NPs were performed in a two-electrode system using 2 M KOH electrolyte. Fig. 4(a) demonstrates the cyclic voltammetry (CV) characteristics of the $Cu_2O$ NCs across a voltage sweep between 0 V and 0.8 V at different scan rates in the range of 10–150 mV. The CV curves of $Cu_2O$ exhibit pairs of anodic and cathodic peaks with a wide redox background, representing the pseudocapacitive behavior of the material. The pseudocapacitance of the $Cu_2O$ is attributed to redox transitions between Cu(I) oxides–Cu(II). The redox reaction for the $Cu_2O$ electrode takes place in the following manner:

$$Cu(I)\ \text{oxide} = Cu(II)\ \text{oxide} + e^{-} \quad (1)$$

At a scan rate of 20 mV $s^{-1}$, weak redox peaks are observed due to residual oxygen-containing groups. The anodic and cathodic peaks correspond to the oxidation and reduction of metal, resulting in electrochemical reactions that take place, as in the following eqn (2):

$$Cu_2O + 2OH^{-} \leftrightarrow 2CuO + H_2O + 2e^{-} \quad (2)$$

As the scan rate increases, the current under the curve gradually rises, which shows that the voltammetry current has a positive relationship with the scan rate. This clearly shows the capacitive behavior of the structure, as can be inferred from the mathematical definition of capacitance, which is the proportional factor between the change in voltage on the capacitor plate and that in the amount of charge, the time integration of the current, on the plate. Also, due to the internal resistance of the electrode and the increase in the scan rate, the current density peak is shifted in performing both forward and subsequent backward sweeps. The capacitive behavior of the Au/$Cu_2O$ composite NPs was characterized by carrying out electrochemical measurements at different scan rates from 20 mV $s^{-1}$ to 150 mV $s^{-1}$, as shown in Fig. 4(b). It can be observed from the CV that the curve is slightly distorted and that the oxidation peaks are slightly shifted with an increase in the scan rate. Another point noted is that Au can easily be oxidized in less acidic solutions, which was experimentally confirmed by the oxidation peaks becoming more prominent as the scan rate increases. In KOH electrolyte, $AuCl_2$ is simply changed into CuO because of the great bonding affinity between $OH^{-}$ and $Cu^{2+}$, while $Cu^{2+}$ remains static on the electrode. The anodic peak (positive current) at 0.1 V signifies an oxidation process associated with $Cu^{+} \rightarrow Cu^{2+}$ (Fig. 4(b)). The peak potentials move to be more anodic with an increase in the scan rate, which is largely associated with internal resistance,[33] however, the shift can only be perceived at a relatively low scan rate of <40 mV $s^{-1}$. Galvanostatic charge–discharge (GCD) measurements were carried out *via* chronopotentiometry from 0 V to 1.2 V at a current density of 2 A $g^{-1}$. Fig. 4(c) shows the repeated

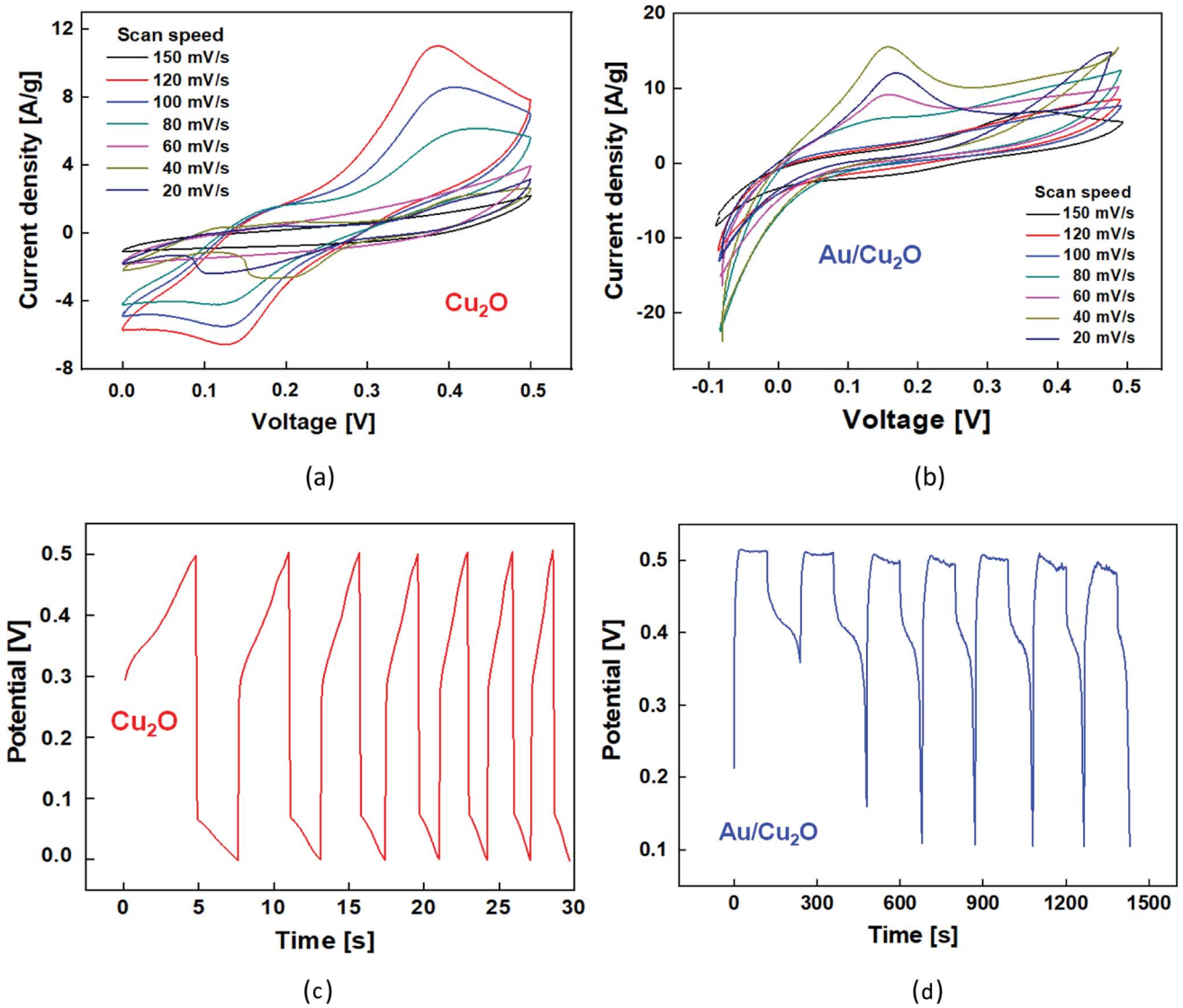


Fig. 4 (a and b) CV curves of the $Cu_2O$ NCs and Au/$Cu_2O$ composite NPs at different scan rates of 10–150 mV $s^{-1}$. (c and d) Galvanostatic charge–discharge (GCD) measurements of the $Cu_2O$ NCs and Au/$Cu_2O$ composite NPs at a current density of 2 A $g^{-1}$.

symmetric triangular shapes observed in the GCD measurements of the $Cu_2O$ NCs and Au/$Cu_2O$ composite NPs.

The charge/discharge peaks are not on an ideal line since the capacitive operation is subordinate to the faradaic redox reaction. The electrode charging begins to be effective at an applied voltage of higher than 0.1 V owing to the oxidation and discharging process of CuO. This signifies a noble interfacial interaction between the active material and the substrate *via* a charge/discharge route. Fig. 4(d) shows the GCD analysis results of the Au/$Cu_2O$ composite NPs at a current density of 2 A $g^{-1}$. The peak digresses from the line discharge method of an EDLC. Thus, this shows that there is a significant increase in the effective surface area of the Au/$Cu_2O$ composite NPs, which leads to a higher capacitance.

The cycling stability of the $Cu_2O$ and Au/$Cu_2O$ composite NP composite electrode electrochemical capacitor upon charge/discharge cycles in 2 M KOH at a current density of 2 A $g^{-1}$ was investigated. Fig. 5 shows the capacitance retention, or, equivalently, the degradation in the specific capacitance ($C_s$) as a function of the number of cycles. The Au/$Cu_2O$ NPs demonstrate a loss in capacitance below 7% even after 10 000 cycles while the $Cu_2O$ NCs show severe degradation of more than 50%. Great electrochemical stability can be expected from the Au/$Cu_2O$ composite in supercapacitor applications. The construction of a porous structure over the shell provides conduction pathways for carriers to enter the core. The heterostructure composed of the Au core and porous shell has a large number of electroactive sites. The capacitance is an electrical parameter defined as the change in the amount of charge per that in the applied voltage on the electrodes on both sides of a capacitor. The effective redox processes taking place in the heterostructure have an effect of sustaining the amount of charge over the cyclic operations so that higher stability against degradation in capacitance can be achieved in the capacitor with electrodes made from Au/$Cu_2O$ NPs.

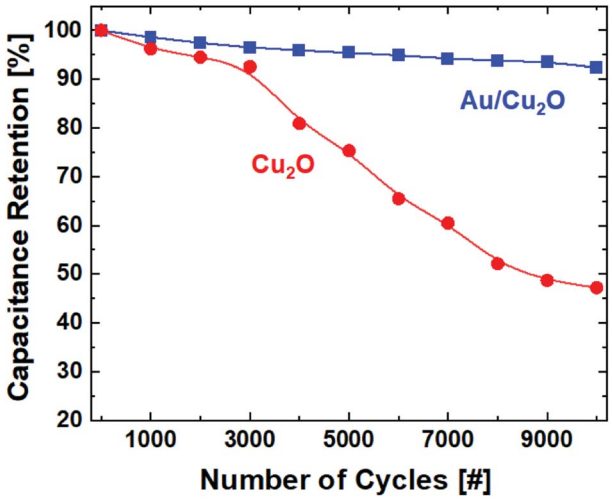


Fig. 5 Cycling stability tests of the $Cu_2O$ NCs and Au/$Cu_2O$ composite NPs.

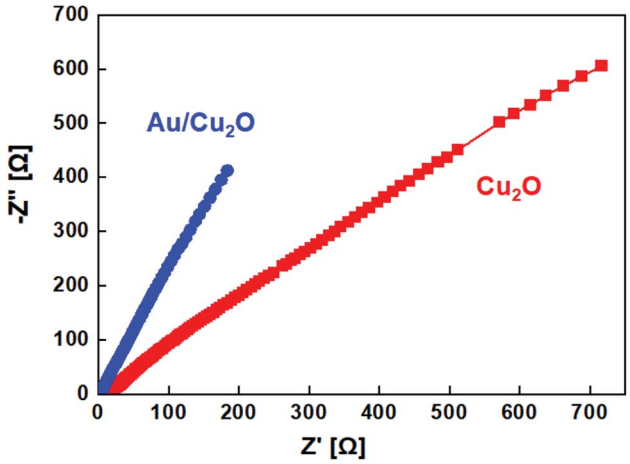


Fig. 6 Electrochemical impedance spectra of the $Cu_2O$ NCs and Au/$Cu_2O$ composite NPs in a frequency range from 10 MHz to 100 kHz.

Furthermore, the charge transfer at the electrode/electrolyte interface was investigated by electrochemical impedance spectroscopy (EIS) in 2 M KOH aqueous electrolyte with a variation in the frequency from 10 MHz to 100 kHz along with the measurement of the electrical conductivity. Fig. 6 shows the Nyquist plots of the EIS spectra of the $Cu_2O$ NCs and Au/$Cu_2O$ composite NPs. A semicircle trajectory is depicted across the high-frequency region and a straight line can be observed in the low-frequency region of the data. The semicircle corresponds to the electron transfer resistance, which is responsible for the electron transfer kinetics of the redox $Cu_2^+$ and $Au_2^+/Cu_3^+$ links at the electrode interface, whereas the linear trajectory in the low-frequency region signifies general capacitive behavior. The semicircle of the Au/$Cu_2O$ composite NPs in the high-frequency region is smaller than that of the $Cu_2O$ NCs, representing reduced charge-transfer resistance, whereas the slant of the line for the Au/$Cu_2O$ composite NPs is greater than that of the $Cu_2O$ NCs, signifying the higher capacitive nature and a lower diffusion resistance of ions in the composite.[34,35] Therefore, the Au/$Cu_2O$ composite NPs have much lower charge transfer resistance and ion diffusion resistance than the $Cu_2O$ NCs, leading to higher reactivity and faster reaction kinetics. The line of the Au/$Cu_2O$ composite NPs in the low-frequency region appears to be sharp, which reveals fast diffusion and relocation of the electrolyte ions. In terms of the oxygen content in the active Au/$Cu_2O$ composite, that of the NPs is higher than that of the $Cu_2O$ NCs; the EIS at the electrode/electrolyte interface is noticeably reduced from 2.2 Ω to 0.65 Ω, correspondingly.[36,37] The lower resistance of the Au/$Cu_2O$ composite NP electrode makes it presumably more conductive, which can be attributed to a higher effective surface area on which there are more active sites for faradaic reactions and electrolyte penetration to take place. Therefore, Au/$Cu_2O$ is more suited for supercapacitor applications due to its high capacitance. The specific capacitance ($C_s$) [F $g^{-1}$] of the electrodes can be calculated using eqn (3):

$$C_s = (I\Delta t)/(m\Delta V) \quad (3)$$

where, $I$, $\Delta t$, and $m$ are the current, discharge time, and mass of the electrode, respectively. $\Delta V$ denotes the potential change during discharge. From the CV curves, the calculated specific capacitances of the $Cu_2O$ NCs and Au/$Cu_2O$ composite were calculated using eqn (3). The high performance of the Au/$Cu_2O$ composite electrode material can be mainly attributed to its unique structure. More specifically, the following are reasons for the underlying physics: (i) the core structure consists of many tiny nanocrystals that have active redox sites which are interconnected and trigger a long discharge process. (ii) The composite has a high effective surface area, which prevents agglomeration and can form pathways for electron transport, and, subsequently, boost the capacitive performance. (iii) Au in the core not only acts as a host for $Cu_2O$ but also prevents stacking. This leads to cooperative behavior with excellent dispersibility in the electrolyte solution and highly effective dissemination of the electrolyte ions *via* porous channels for redox reactions. At the same time, the charge storage capability is enhanced. Notably, the specific capacitance of the Au/$Cu_2O$ composite is one of the most prominent electrochemical performances among graphene-based $Cu_2O$ reported materials, as shown in Table S1.† Fig. 7 shows the $C_s$ as a function of the scan rate. The reduction in $C_s$ at a high scan rate is due to the redox reaction at the electrode/electrolyte interface. These $C_s$ values at different scan rates can be correlated with the results of the CV measurements shown in Fig. 4(a)–(d). The capacitances of the $Cu_2O$ NCs and Au/$Cu_2O$ composite NPs decrease with increasing discharge current density, however, the capacitance of the Au/$Cu_2O$ composite NPs is higher than that of the $Cu_2O$ NCs at all current densities and scan rates, as demonstrated in Fig. 7. The average $C_s$ values of $Cu_2O$ NCs and Au/CuO composite NPs are 140 F $g^{-1}$ and 235 F $g^{-1}$, respectively, at a current density of 2 A $g^{-1}$. These outstanding performances are comparable to those of previously reported electrodes shown in Table S1.[38]† These results indicate that the Au/$Cu_2O$ composite NP electrode with an improved $C_s$ can be largely

attributed to the major role played by the novel core–shell NP structure, which substantially acts as an active material supporting both the AuNRs and $Cu_2O$ NPs. It has been proven that the Au/$Cu_2O$ composite NPs provide a higher $C_s$ value towards application in a supercapacitor. To realize a high-performance supercapacitor owing to a synergistic effect, we designed a core–shell nanostructured Au core $Cu_2O$ shell on Ni foam. AuNRs serve as a conductive layer for electron transport while $Cu_2O$ allows fast ion diffusion owing to its large interlayer spacing. The synergistic effect of the material arises from the combination of the AuNRs (good electrical conductivity) and $Cu_2O$ (large interlayer spacing). In summary, this design of a binder-free electrode enhances the ion diffusion as well as electron transport at the electrode/electrolyte interface. The core–shell nanoparticles of different shapes provide a short diffusion path and high active surface area for ions and electrons and may produce a synergistic effect on each component, resulting in high capacitance, low internal resistance, remarkable rate capability, and excellent stability.

# 4. Experimental

## 4.1 Materials and reagents

All the chemicals were of analytical grade and used without purification. Gold(III) chloride trihydrate ($HAuCl_4 \cdot 3H_2O$ 99.9%), cetyltrimethylammonium bromide (CTAB 99%), D-glucosamine, silver nitrate ($AgNO_3$ 99.9%), copper(II) chloride ($CuCl_2$), sodium borohydride ($NaBH_4$ 99%), L-ascorbic acid (AA 99.8+%), copper(II) nitrate hemi-pentahydrate ($2Cu(NO_3)_2 \cdot 5H_2O$), and ethanol were obtained from Sigma Aldrich Korea. Sodium hydroxide (98.9+%) and L-glutamic acid were purchased from Dae-Jung Chemical. All of the experiments were conducted in purified water with 18 mQ resistance.

## 4.2 Synthesis of the AuNRs

AuNRs were prepared using a typical seed-mediated growth approach following a modified literature preparation.[20] Firstly, a seed mixture was made by adding 0.45 mL of $HAuCl_4 \cdot 3H_2O$ (0.01 M) to 8.57 mL of CTAB (0.1 M) solvent, and then to this mixture, 0.7 mL of freshly prepared cold sodium borohydride (0.01 M) solution was rapidly added under magnetic stirring for 15 min. The color of the resultant mixture changed to a light brownish one. The mixture was then left to stand for 5 h to complete the formation of the seed mixture. Furthermore, 100 mL of growth solution was prepared by adding 5 mL of $HAuCl_4 \cdot 3H_2O$ (0.01 M) and 95 mL of CTAB (0.1 M) solution. 0.6 mL of 0.01 M $AgNO_3$ solution was added to the mixture under stirring to control the outgrowth of AuNRs. Then, 0.65 mL of L-ascorbic acid (0.1 M) was added in a dropwise manner and the resulting mixture turned colorless. 140 μL of the seed-mediated mixture was then added to the growth mixture. The growth solution slowly transformed into a light blue color over 10 min. The resultant solution was left overnight for maximal growth. Finally, the mixture was centrifuged at a speed of 13 000 revolutions per minute (rpm) for 20 min.

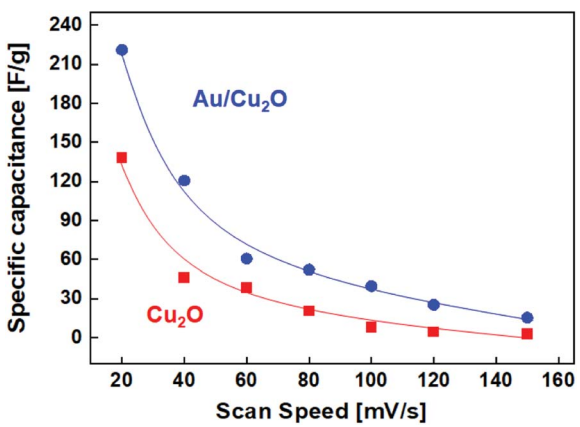


Fig. 7 Average specific capacitance ($C_s$) of the $Cu_2O$ NCs and Au/$Cu_2O$ composite NPs at different scan rates.

## 4.3 Synthesis of the $Cu_2O$ NCs

$Cu_2O$ NCs were synthesized *via* the reduction of copper nitrate with L-ascorbic acid following a modified literature protocol.[18] 0.003 M $Cu(NO_3)_2 \cdot 5H_2O$ was liquefied in 90 mL of double-distilled ultrapure water. Afterward, 0.4 M sodium hydroxide solutions were prepared in different vials. 0.05 M L-ascorbic acid solution was also prepared in 10 mL of water. Copper nitrate solution was stirred for 15 min and its light blue color turned into dusky blue after adding sodium hydroxide solution. Finally, a cherry-red colored mixture was observed, and, subsequently, the dropwise addition of L-ascorbic acid and stirring for 30 min led to the final solution color turning to bright yellow, confirming the formation of the $Cu_2O$ NCs, as supported by the EDX analysis shown in Fig. S1.† The obtained solution was purified repeatedly using ethanol and water after aging for 20 min and kept overnight under a vacuum pump to obtain a completely dry powder.

## 4.4 Synthesis of the Au/$Cu_2O$ NPs

The Au/$Cu_2O$ composite NPs were synthesized in aqueous solution. 0.125 g of SDS was mixed in 80 mL of 0.004 M $CuCl_2$, then 5.0 mL of the AuNR solution was added into the above mixture in a dropwise manner. Afterward, 10 mL of 0.4 M sodium hydroxide solution was slowly added to it and rapidly stirred at room temperature for 15 min. Subsequently, 10 mL of 0.04 M ascorbic acid solution was added dropwise. The color transformed from blue to yellowish-green, evidence of the formation of the Au/$CuO_2$ NPs. Finally, the mixture was centrifuged at 5000 rpm in water and ethanol three times, respectively, before being subjected to 45 min of aging. The precipitate was re-dispersed in ethanol for additional use. The synthesis procedures were completed using Au/$Cu_2O$ composite NPs with a final weight ratio of 4.1 between Au and $Cu_2O$.

# 5. Conclusions

The chemical synthesis of the $Cu_2O$ NCs and Au/$Cu_2O$ composite NPs featuring an AuNR core and $Cu_2O$ shell is herein

reported. From the TEM and XRD analysis results, it was confirmed that the as-synthesized material contains AuNRs in the core and $Cu_2O$ as the shell and that both materials are highly crystalline. The Au/$Cu_2O$ NPs exhibit a core–shell structure in which the AuNRs are embedded as the core surrounded by a $Cu_2O$ cubic shell. It is understood that the mass of Au added in the synthesis route plays a major role in controlling the NP size, resulting in Au/$Cu_2O$ NPs with different shell thicknesses being obtained as a result. More significantly, the Au/$Cu_2O$ composite NPs are crystalline, with a high specific surface area of 1150.760 $m^2 g^{-1}$. Furthermore, these nanoscale architectures were used in a device towards application as a supercapacitor. The Au/$Cu_2O$ composite NPs exhibit a high specific capacitance of 235 F $g^{-1}$ at a current density of 2 A $g^{-1}$ in 2 M aqueous KOH electrolyte, which is greater than that of $Cu_2O$, at 140 F $g^{-1}$. It has thus been confirmed that the Au/$Cu_2O$ composite is a promising electrode material for use in high-performance supercapacitors.

## Conflicts of interest

There are no conflicts to declare.

## Acknowledgements

This work was supported by the National Research Foundation of Korea (NRF) through a Research Grant funded by the Korean Ministry of Science and ICT (MSIT) under the Grant No. 2021M3H4A6A01048300.

## References

1 M. Li, J. Cheng, J. Wang, F. Liu and X. Zhang, *Electrochim. Acta*, 2016, **206**, 108–115.
2 J. Suntivich, H. A. Gasteiger, N. Yabuuchi and Y. Shao-Horn, *J. Electrochem. Soc.*, 2010, **157**, B1263–B1268.
3 X. Wang, X. Han, M. Lim, N. Singh, C. L. Gan, M. Jan and P. S. Lee, *J. Phys. Chem. C*, 2012, **116**, 12448–12454.
4 A. K. Singh, D. Sarkar, K. Karmakar, K. Mandal and G. Khan, *ACS Appl. Mater. Interfaces*, 2016, **8**, 20786–20792.
5 C. Lamiel and J. J. Shim, *New J. Chem.*, 2016, **40**, 4810–4817.
6 S. Wang, L. Jiang, L. Hu, Q. Wang, S. Zhan and Y. Lu, *J. Alloys Compd.*, 2020, **815**, 1520105.
7 J. Yan, Z. Fan, T. Wei, W. Qian, M. Zhang and F. Wei, *Carbon*, 2010, **48**, 3825–3833.
8 V. Subramanian, H. Zhu and B. Wei, *J. Power Sources*, 2006, **159**, 361–364.
9 H. Zang, Y. Tian, S. Wang, Y. Huang, J. Wen, C. Hang and C. Wang, *Chem. Eng. J.*, 2020, **399**, 125–175.
10 X. Du, C. Wang, M. Chen, Y. Jiao and J. Wang, *J. Phys. Chem. C*, 2009, **113**, 2643–2646.
11 S. Z. Golkhatmi, M. Khalaj, A. Izaspanahi and A. Sedghi, *Solid State Sci.*, 2015, **106**, 1060336.
12 K. K. Purushothaman, B. Saravanakumar, I. M Babu, B. Sethuraman and G. Muralidharan, *RSC Adv.*, 2014, **4**, 23485–23491.
13 I. Y. Bu and R. Huang, *Ceram. Int.*, 2016, **43**, 45–50.
14 A. Pendashteh, M. S. Rahmanifar and M. F. Mousavi, *Ultrason. Sonochem.*, 2014, **21**, 643–652.
15 J. F. Juni, S. R Majid, S. N. F. Yusuf and Z. Osman, *Microchem. J.*, 2021, **164**, 106–155.
16 H. Zhou, G. Han, Y. Xiao, Y. Chang and H. J. Zhai, *J. Power Sources*, 2014, **263**, 259–267.
17 C. Chaojing, L. Aifeng, L. Yanei, M. Jingbo, Z. Xiaoliang and C. Hongwei, *Mater. Lett.*, 2017, **196**, 308–311.
18 M. Yu, Y. Ma, J. Liu and S. Li, *Carbon*, 2015, **87**, 98–105.
19 Q. Cheng, J. Tang, J. Ma, H. Zhang, N. Shinya and L. C. Qin, *J. Phys. Chem. C*, 2011, **115**, 23584–23590.
20 M. H. Bai, T. Y Liu, F. Luan, Y. Li and X. X. Liu, *J. Mater. Chem. A*, 2014, **2**, 10882–10888.
21 X. Zheng, L. Miao, Z. Song, W. Du, D. Zhu, Y. Lv, L. Li, L. Gan and M. Liu, *J. Mater. Chem. A*, 2022, **10**, 611–621.
22 D. P. Dubal, S. H. Lee, J. G. Kim, W. B. Kim and C. D. Lokhande, *J. Mater. Chem.*, 2012, **22**, 3044–3052.
23 K. Shi, X. Pang and I. Zhitomirsky, *J. Mater. Sci. Technol.*, 2020, **55**, 182–189.
24 C. Pirvu, C. C. Manole, A. B. Stoian and I. Demetrescu, *Electrochim. Acta*, 2011, **56**, 9893–9903.
25 K. Shi and I. Zhitomirsky, *J. Power Sources*, 2013, **240**, 42–49.
26 K. K. Sourav, R. Debdhutta and C. R. Somnath, *J. Alloys Compd.*, 2022, **895**, 1620546.
27 Z. Song, L. Miao, L. Ruhimann, Y. Lv, D. Zhu, L. Li, L. Gan and M. Liu, *Adv. Mater.*, 2021, **33**, 2104148.
28 K. Mukesh, C. Himani, S. Biswarup and D. Sasanka, *Z. Phys. Chem.*, 2019, **233**, 85–104.
29 S. Shahrokhian, Z. Kamalzadeh and R. S. Saberi, *Electroanal*, 2011, **23**, 2925–2934.
30 Y. Song, T. Y. Liu, X. X. Xu, D. Y. Feng, Y. Li and X. X. Liu, *Adv. Funct. Mater.*, 2015, **25**, 4626–4632.
31 G. Mitchell, F. Davis and C. Legge, *Synth. Met.*, 1988, **26**, 247–257.
32 Y. Jiang, J. Chen, X. Zhao and G. Ma, *Catalysts*, 2021, **11**, 600.
33 J. Chen, H. Liu, X. Wan, X. Xue, Y. Zhang, Y. Liu and A. Yuan, *J. Nanopart. Res.*, 2019, **21**, 1–10.
34 T. Liu, L. Finn, M. Yu, H. Wang, T. Zhai, X. Lu, Y. Tong and Y. Li, *Nano Lett.*, 2014, **14**, 2522–2527.
35 C. Yang, L. Zhang, N. Hu, Z. Yang, H. Wei and Y. Zhang, *J. Power Sources*, 2016, **302**, 39–45.
36 S. Lyu, H. Chang, F. Fu, L. Hu, J. Huang and S. Wang, *J. Power Sources*, 2016, **327**, 438–446.
37 M. Shoeb, M. Mobin, S. M. Adan, I. F. Ansari, M. N. Khan, S. Zaidi and M. Y. Ansari, *Surf. Interfaces*, 2022, **28**, 101650.
38 Z. Zhou, L. Miao, H. Duan, Z. Wang, Y. Lv, W. Xiong, D. Zhu, L. Li, M. Liu and L. Gan, *Chin. Chem. Lett.*, 2020, **31**, 1226–1230.